NEURAL REGENERATION RESEARCH
www.nrronline.org

Research Article

Reduced graphene oxide-embedded nerve conduits loaded with bone marrow mesenchymal stem cell-derived extracellular vesicles promote peripheral nerve regeneration

Wei Zhang[1, 2], Xing-Xing Fang[1, 2], Qi-Cheng Li[1, 2], Wei Pi[1, 2], Na Han[1, 2, 3, *]

https://doi.org/10.4103/1673-5374.343889

Date of submission: November 6, 2021

Date of decision: January 13, 2022

Date of acceptance: February 25, 2022

Date of web publication: April 25, 2022

From the Contents

Graphical Abstract

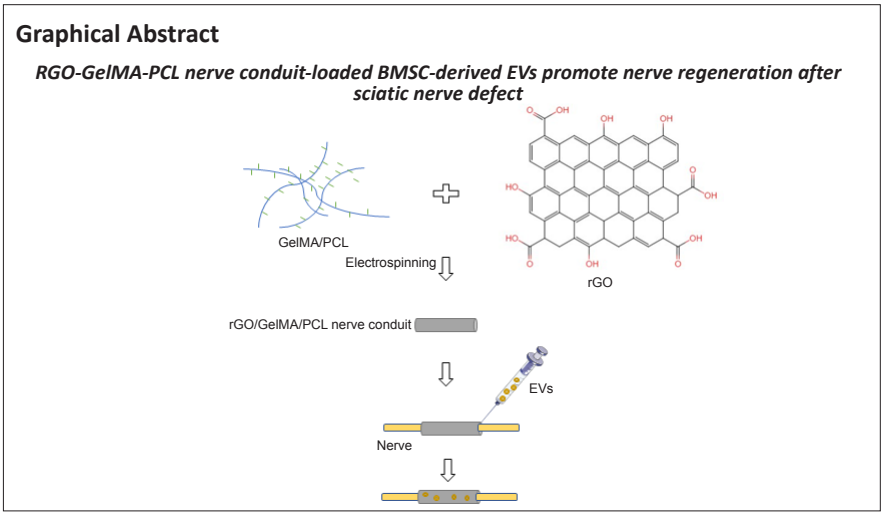

Abstract

We previously combined reduced graphene oxide (rGO) with gelatin-methacryloyl (GelMA) and polycaprolactone (PCL) to create an rGO-GelMA-PCL nerve conduit and found that the conductivity and biocompatibility were improved. However, the rGO-GelMA-PCL nerve conduits differed greatly from autologous nerve transplants in their ability to promote the regeneration of injured peripheral nerves and axonal sprouting. Extracellular vesicles derived from bone marrow mesenchymal stem cells (BMSCs) can be loaded into rGO-GelMA-PCL nerve conduits for repair of rat sciatic nerve injury because they can promote angiogenesis at the injured site. In this study, 12 weeks after surgery, sciatic nerve function was measured by electrophysiology and sciatic nerve function index, and myelin sheath and axon regeneration were observed by electron microscopy, immunohistochemistry, and immunofluorescence. The regeneration of microvessel was observed by immunofluorescence. Our results showed that rGO-GelMA-PCL nerve conduits loaded with BMSC-derived extracellular vesicles were superior to rGO-GelMA-PCL conduits alone in their ability to increase the number of newly formed vessels and axonal sprouts at the injury site as well as the recovery of neurological function. These findings indicate that rGO-GelMA-PCL nerve conduits loaded with BMSC-derived extracellular vesicles can promote peripheral nerve regeneration and neurological function recovery, and provide a new direction for the curation of peripheral nerve defect in the clinic.

Key Words: angiogenesis; axon; bone mesenchymal stem cell; extracellular vesicles; hybrid nanofibers; myelin sheath; nerve conduit; neurological function; peripheral nerve injury; reduced graphene oxide

Introduction

Peripheral nerve injury often results in increased patient suffering from long-standing disabilities, such as loss of sensory and/or motor function and neuropathic pain, which create a substantial socio-economic burden (Duarte-Moreira et al., 2018; Fang et al., 2020b; Li et al., 2021; Qu et al., 2021). Autologous nerve transplantation is the current gold standard for treatment of long peripheral nerve defects; however, this method is limited because of the lack of donor nerves (Griffin et al., 2013). Previous studies have demonstrated that nerve conduits are a promising technique for bridging damaged nerve stumps when autologous nerve transplantation is not possible (Zou et al., 2020; Pozzobon et al., 2021; Zaminy et al., 2021).

The nervous system relies on electrical conductivity generated by ion flow to coordinate cellular function and signal transduction (McCaig et al., 2005). Recent studies have shown that the electrical conductivity of nerve conduits can effectively promote neurite and axon extension *in vitro* and nerve regeneration *in vivo* (Geetha Bai et al., 2018; Wang et al., 2019). Graphene has become a research hotspot in the field of biomaterials because of its unique electrical and mechanical flexibilities (Farokhi et al., 2021). Reduced graphene oxide (rGO) is an important derivative of graphene. Compared with graphene, rGO has lower cytotoxicity, while maintaining good conductivity (Liu et al., 2017). To generate rGO nerve conduits with greater biocompatibility, we introduced gelatin-methacryloyl (GelMA) into the underlying substrate of the conduit. As a protein derivative, GelMA has good biocompatibility and can bind cells and enhance cell-mediated matrix degradation through its internal arginine-glutathione adhesion domain and matrix metalloproteinase sensitive sites (Khayat et al., 2017). In the cardiovascular system, which is another type of electrically active tissue, rGO-GelMA hydrogels demonstrated good biocompatibility and conductivity (Lee et al., 2019). However, because of the lack of mechanical properties, rGO-GelMA hydrogels cannot be directly applied to peripheral nerve regeneration. Polycaprolactone (PCL) has been widely used in tissue engineering because of its excellent mechanical properties and biodegradability (Siddiqui et al., 2018). We fabricated nerve conduits by electrospinning the substrates rGO, GelMA, and PCL. Combining the conductivity of rGO, biocompatibility of GelMA, and the mechanical

[1]Department of Orthopedics and Trauma, Peking University People's Hospital, Beijing, China; [2]National Center for Trauma Medicine, Beijing, China; [3]Central Laboratory, Peking University People's Hospital, Beijing, China

*Correspondence to: Na Han, PhD, hannaqa@hotmail.com.cn.

https://orcid.org/0000-0002-5099-714X (Wei Zhang)

Funding: *This work was supported by the National Natural Science Foundation of China, No. 31671248 and the Natural Science Foundation of Beijing, No. 7222198 (both to NH).*

How to cite this article: *Zhang W, Fang XX, Li QC, Pi W, Han N (2023) Reduced graphene oxide-embedded nerve conduits loaded with bone marrow mesenchymal stem cell-derived extracellular vesicles promote peripheral nerve regeneration. Neural Regen Res 18(1):200-206.*

properties of PCL, the rGO-GelMA-PCL nerve conduits promoted better nerve function recovery than non-conductive nerve conduits (Fang et al., 2020a). However, a gap in nerve function recovery and nerve regeneration still exists between the efficacy of nerve conduits and autologous nerve transplantation.

Bone marrow mesenchymal stem cells (BMSCs) have been studied widely in the field of tissue regeneration for repair of bone defects, cerebral ischemia, and peripheral nerve injury (Zhang et al., 2016, 2017; Adameyko and Ernfors, 2019). However, the source of BMSCs is limited and their capacity to differentiate into osteocytes and chondrocytes can induce calcification in the injected areas (Breitbach et al., 2007; Sun et al., 2016). Moreover, direct transplantation of mesenchymal stem cells was reported to potentiate tumor growth (Zhu et al., 2011). Extracellular vesicles (EVs) are secreted by cells, and their diameters range between 30–200 nm (Yu et al., 2014). The substances inside EVs include proteins, micro RNA, mRNA, and lipids, which are involved in cell-to-cell communication and play an important role in the progression of tissue regeneration (Phinney and Pittenger, 2017). In addition, BMSC-derived EVs can accelerate tissue regeneration by promoting angiogenesis (Brennan et al., 2020). Therefore, BMSC-derived EVs can promote regeneration similar to BMSCs and overcome the limitations of BMSC transplantation therapy. BMSC-derived EVs can be used for cell-free regenerative medicine and potential application for wound healing and neurological disease and injury (Xin et al., 2012; Rani and Ritter, 2016).

The excellent biocompatibility and low cytotoxicity of the rGO-GelMA-PCL nerve conduit create a suitable microenvironment for nerve regeneration (Fang et al., 2020a). BMSC-derived EVs may activate nerve regeneration by cell-to-cell communication and the promotion of angiogenesis. Complex reparation materials are more likely to create an improved microenvironment that promotes nerve regeneration (Zhang et al., 2018). In this study, we hypothesized that the regeneration-promoting effect of rGO-GelMA-PCL nerve conduits could be combined with the angiogenesis-promoting effect of BMSC-derived EVs to improve nerve regeneration and functional recovery. Therefore, we combined BMSC-derived EVs with rGO-GelMA-PCL nerve conduits and explored their role in the treatment of nerve defects in rats.

Methods

Animals

BMSCs were isolated from three 2-day-old (weighing 5.5–10 g) and two 8-week-old (weighing 180–200 g) male or female Sprague-Dawley rats. To avoid high aggression by male rats during the assays (Bueno et al., 2017), twenty-four 8-week-old female Sprague-Dawley rats weighing 180–200 g (n = 8/group) were used for the *in vivo* study. The rats were purchased from Beijing Vital River Laboratory Animal Technology Co., Ltd. (Beijing, China; license No. SCXK (Jing) 2016-0006). The rats were feeding in specific-pathogen-free animal laboratory, and the environment was kept quiet, the temperature was controlled between 20–25°C, the humidity was controlled between 50–65%, and the light cycle was 12 hours of light and 12 hours of darkness. All experiments were approved by the Animal Ethics Committee of Peking University People's Hospital (approval No. 2019PHE040) on November 8, 2019. All experiments were designed and reported in accordance with the Animal Research: Reporting of *In Vivo* Experiments (ARRIVE) guidelines (Percie du Sert et al., 2020).

Culture and characterization of rat BMSCs

Briefly, 2-day-old rats were sacrificed by decapitation after anesthetization by 1% isoflurane inhalation (500 mL/min; RWD Life Science; Shenzhen, China), and 8-week-old rats were sacrificed by cervical dislocation after anesthetization by 3% isoflurane inhalation (500 mL/min). The femur, tibia, and humerus bones were removed from each rat and cleaned, and the BMSCs were flushed out as previously described (Xu et al., 2017). The cells were cultured in low glucose Dulbecco's Modified Eagle Medium (GIBCO; Grand Island, NY, USA; Cat# 11885-084) containing 10% fetal bovine serum (GIBCO, Cat# 10099-141) and 1% penicillin-streptomycin (GIBCO, Cat# 15140-122). When the cell fusion confluence reached 50%, the primary cells were passaged at a split ratio of 1:1 (Rao et al., 2019). After the initial passage, the BMSCs were passaged when they reached 80% confluency and split at a ratio of 1:2. Passage numbers 3–5 were used for the identification of the BMSCs (Kim et al., 2020). Flow cytometric analysis was used to identify BMSC-specific surface markers (Sun et al., 2013) using the following fluorochrome-conjugated antibodies: fluorescein isothiocyanate (FITC) anti-rat CD90 (Biolegend, San Diego, CA, USA, Cat# 206105, RRID: AB_2566265), FITC anti-rat CD44 (Biolegend, Cat# 203906, RRID: AB_2076441), phycoerythrin anti-rat CD29 (Biolegend, Cat# 102207, RRID: AB_312884), FITC anti-rat CD45 (Biolegend, Cat# 202205, RRID: AB_314005), and FITC anti-rat CD34 (eBioscience, San Diego, CA, USA, Cat# 11-0341-82, RRID: AB_465021). Adipogenic, osteogenic, and chondrogenic lineage differentiation media were used to characterize the multidirectional differentiation potential of the cultured cells. Briefly, mesenchymal stem cells were cultured for 14 days in adipogenic induction medium for oil red O staining (Cyagen, Guangzhou, China; RAXMX-90021), 21 days in osteogenic induction medium for alizarin red staining (Cyagen, Cat# RAXMX-90031), and 21 days in chondrogenic induction medium for alcian blue staining (Cyagen, Cat# RAXMX-90041). The cells were observed and photographed using a light microscope (Leica, Wetzlar, Germany) (Sun et al., 2013).

Isolation and characterization of EVs from cell culture supernatants

Fetal bovine serum was ultracentrifuged at 100,000 × g at 4°C for 24 hours to remove EVs. The EV-free complete medium contained low glucose Dulbecco's modified Eagle medium, 10% EV-free fetal bovine serum, and 1% penicillin-streptomycin. After the 3rd or 4th generation of BMSCs reached 90% confluency, the cells were rinsed with phosphate-buffered saline (PBS), and the EV-free complete medium was added. After 48 hours, a 500 mL cell culture supernatant (1×10^6 cells/mL culture supernatant) was collected. EVs were isolated from the BMSC culture supernatant by differential centrifugation (He et al., 2020). First, the cell culture supernatant was centrifuged at 300 × g for 10 minutes at 4°C to eliminate the living cells. Then, the supernatant was collected and centrifuged at 4°C for 10 minutes at 2000 × g to eliminate dead cells. After that, the supernatant was collected again and centrifuged at 10,000 × g for 30 minutes at 4°C to remove cellular debris. The final supernatant was ultracentrifuged at 100,000 × g at 4°C for 70 minutes. The supernatant was discarded carefully and the precipitate was resuspended in PBS. The resuspended precipitate was ultracentrifuged at 100,000 × g for 70 minutes at 4°C. The final precipitate was resuspended in 200 µL PBS to obtain EVs (Théry et al., 2006). EVs from 8-week-old rat BMSCs were only used in the tube formation assay to compare the tube promoting effects between EVs from neonatal and older rats. The other assays used EVs derived from 2-day-old rat BMSCs. The bicinchoninic acid (BCA) Protein Assay Kit (Solarbio, Beijing, China; PC0020) was used to determine the concentration of EVs (Ma et al., 2019). Five µL of each standard protein solution and 5 µL of the exosome preparation were added to separate wells of a 96-well plate, 300 µL of BCA working solution was added to each well, and the plate was incubated at 37°C for 30 minutes. The absorbance at 563 nm was measured with a microplate reader (Bio-Rad, Hercules, CA, USA), and a standard curve was generated from the absorbance values of the standard protein solutions. The concentration of exosomes was determined according to the absorbance and the standard curve. A transmission electron microscope (JEOL, Tokyo, Japan; JEM-1230) was used to observe the appearance of BMSC-derived EVs. The particle size was analyzed by nanoparticle tracking analysis. Western blot was used to determine the membrane markers on the isolated EVs, and the antibodies included rabbit anti-CD9 (1:1000; BIOSS, Beijing, China, Cat# bs-22293R, RRID: AB_2895670) and rabbit anti-tumor susceptibility gene 101 (TSG101; 1:1000; BIOSS, Cat# bsm-52746R, RRID: AB_2895671).

The uptake of BMSC-derived EVs by human umbilical vein endothelial cells

PKH26 (Sigma; Darmstadt, Germany; Cat# MINI26) was used to label EVs as previously reported (He et al., 2020). Briefly, 50 µL PKH26 working regent was added per 100 µg EVs and incubated at room temperature for 10 minutes. The excess dye was removed by ultracentrifugation at 100,000 × g for 70 minutes. The labeled EVs were added to a culture dish containing human umbilical vein endothelial cells (HUVECs; American Type Culture Collection, Manassas, VA, USA; ATCC Cat# CRL-1730, RRID: CVCL_2959) that had reached approximately 30% confluency. Twenty-four hours later, the HUVECs were rinsed twice with PBS after which Actin-Tracker Green (Beyotime, Shanghai, China, Cat# C2201S) was used to stain the cytoskeleton and 4′,6-diamidino-2-phenylindole dihydrochloride (DAPI; Sigma, Cat# D9524) was used to stain nuclei. The uptake of BMSC-derived EVs was observed by fluorescence microscopy (Leica).

Tube formation assay

In accordance with the Matrigel Basement Membrane Matrix instructions (BD, San Jose, CA, USA; Cat# 356234), 2×10^4 HUVECs were added into each well of a 96-well cell culture plate coated with Matrigel™. Then, 0.16 mm^2 rGO-GelMA-PCL hybrid nanofibers were added to each of these wells followed by the addition of 0 or 20 µg EVs in 20 µL PBS per well. After 6 hours, tube formation was observed using a light microscope (Leica). Five microscopic fields were randomly selected, and the tube lengths were calculated using Image-Pro Plus 6.0 software (Media Cybernetics, Rockville, MD, USA).

Animal surgery

The rGO-GelMA-PCL nerve conduit was synthesized by our laboratory as previous described (Fang et al., 2020a). Briefly, the rGO-GelMA-PCL compound (0.5 wt% rGO) was ejected onto a 1.2 mm stainless steel rod by an electrostatic spinning machine (IonBeam, Beijing, China, Cat# WL-2C) at a rate of 2 mL/h. After 3 days of vacuum drying, the rGO-GelMA-PCL nerve conduit was completed by removing the steel rod.

Twenty-four rats were divided randomly into three groups: (1) the rGO-GelMA-PCL nerve conduit only group (control group, n = 8); (2) the nerve conduit + BMSC-derived EVs (EV group, n = 8); and (3) the autograft nerve group (autograft group, n = 8) (**Figure 1**). Before surgery, the rats were anesthetized by 3% isoflurane inhalation. The sciatic nerve on the right side was exposed under aseptic conditions, and 7 mm of sciatic nerve was excised between the lower edge of the piriformis muscle and the sciatic nerve bifurcation to create a 10 mm nerve defect model (Li et al., 2016; Saeki et al., 2018). Without an implant, a 10 mm sciatic nerve defect in a rat will form a neuroma and will not self-repair (Sinis et al., 2007). The proximal and distal stumps of the sciatic nerve were pulled 1.5 mm into each end of the nerve conduit and sutured, leaving a 10 mm gap in the middle of the conduit (Wang et al., 2020c). In the control and EV groups, the rGO-GelMA-PCL nerve conduit was used to bridge the 10 mm nerve defect. In the EV group, 20 µg EVs in 20 µL PBS were injected into the conduits using a microinjector (Hamilton; Bonaduz, Switzerland). In the autograft group, 10 mm of sciatic nerve was dissected and then reversed to connect the distal and proximal nerve stumps. The muscles and skin of all groups were sutured with 4-0 nylon sutures (Jinhuan, Shanghai, China).

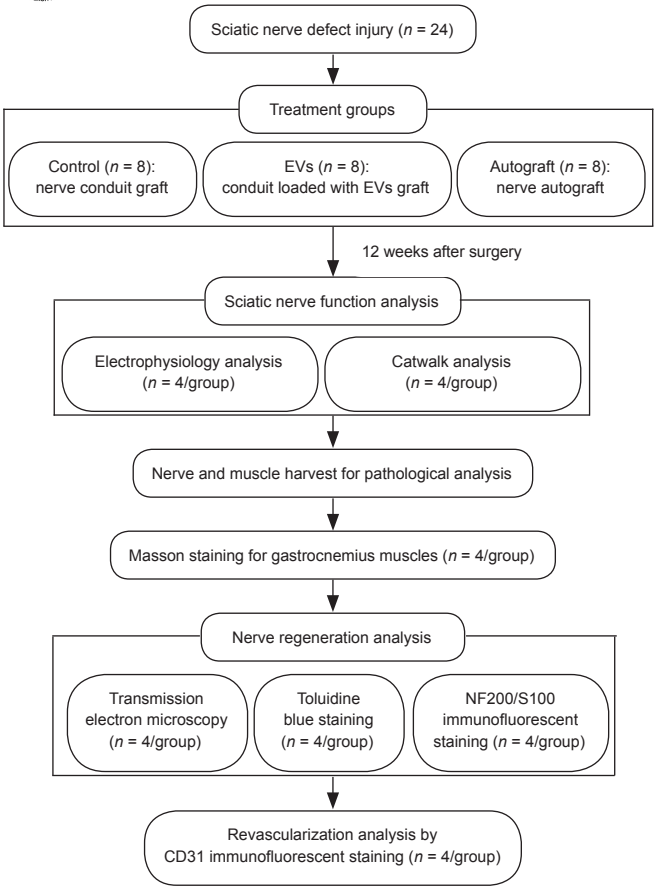

Figure 1 | **A flow chart of the study.**
EVs: Extracellular vesicles; NF200: neurofilament 200.

Functional and electrophysiological assessments

At 12 weeks after surgery, the CatWalk XT (Noldus, Wageningen, Netherlands) gait analysis system was used to evaluate the recovery of motor function in the rats. Briefly, the cameras were fixed under the runway, the focus was adjusted, and the rats were placed in sequence to record their footprints as they passed across the runway. According to the footprints, the sciatic functional index (SFI) was analyzed using the following formula: SFI = 109.5(ETS – NTS)/NTS – 38.3(EPL – NPL)/NPL + 13.3(EIT – NIT)/NIT – 8.8, where EPL indicates the paw length on the operated limb (experimental); NPL indicates the normal paw length; ETS indicates the experimental toe spread; NTS indicates the normal toe spread; EIT indicates the experimental intermediary toe spread; and NIT indicates the normal intermediary toe spread (Erdal et al., 2022).

After the Catwalk analysis, the rats were anesthetized by 3% isoflurane inhalation and the sciatic nerves were exposed. A stimulating electrode was placed at the proximal part of the sciatic nerve 5 mm from the surgical excision site, and two recording electrodes were placed separately at the two ends of the gastrocnemius muscle. The stimulating parameters were set at 0.09 mA and 0.1 ms. After each stimulation, the motor nerve conduction velocity and compound muscle action potential were recorded (Xu et al., 2014).

Muscle evaluation

At 12 weeks after surgery, the gastrocnemius muscles from the operated and contralateral limbs were removed, their wet weights were measured, and the wet weight ratio (operated/contralateral side) was calculated. The muscle specimens were fixed in 4% paraformaldehyde for 12 hours and embedded in paraffin. The specimens were sectioned consecutively at a thickness of 7 μm using a paraffin slicing machine (Leica). The sections were stained with Masson's trichrome (Solarbio, Cat# G1340) in accordance with the manufacturer's instructions. Briefly, sections were stained with Weigert hematoxylin solution for 5 minutes, Masson's bluing solution for 5 minutes, ponceau-acid fuchsin solution for 5 minutes, and aniline blue solution for 2 minutes. Then, the sections were dehydrated in anhydrous ethanol, sealed with neutral gum, and observed with a bright-field microscope (Leica) (Dong et al., 2021). The cross-sectional areas of the muscle fibers were analyzed quantitatively using Image-Pro Plus 6.0 software.

Transmission electron microscopy and morphological analyses

The conduit in which the nerve regenerated was dissected and collected. After fixing with 2.5% glutaraldehyde for 24 hours, the nerve was peeled off of the conduit, stained with 1% osmium acid (Electron Microscopy Sciences, Hatfield, PA, USA), and dehydrated with gradient concentrations of acetone. The samples were embedded in epoxy resin and cut into 700 nm, thick semi-thin and 70 nm-thick ultrathin sections. The semi-thin sections were stained with 1% toluidine blue (Solarbio) to calculate the nerve fiber density, and the ultrathin sections were dyed with uranyl acetate (Electron Microscopy China, Beijing, China) and lead citrate (Electron Microscopy China) to measure myelin sheath thickness and diameter of myelinated axons by transmission electron microscopy. The data were analyzed with Image-Pro Plus 6.0 software.

Immunofluorescence

The regenerated nerves were fixed with 4% paraformaldehyde for 24 hours and cryoprotected with increasing concentrations of sucrose (10%, 20%, and 30%). The samples were embedded in optimal cutting temperature compound and cut into 12 μm-thick sections using a cryostat (Leica). The sections were permeabilized with 0.2% Triton X-100, blocked with 10% goat serum, and incubated at 4°C overnight with rabbit anti-S100 antibody (1:400; Sigma-Aldrich, Cat# S2644, RRID: AB_477501) and mouse anti-neurofilament (NF200; 1:400; Sigma-Aldrich, Cat# N0142, RRID: AB_477257) antibody or rabbit anti-CD31 (1:400; Sigma-Aldrich, Cat# SAB4503968, RRID: AB_2895674) antibody. After rinsing with PBS, the sections were incubated with Alexa Fluor 555-conjugated goat anti-rabbit IgG H+L (1:2000; Cell Signaling Technology, Cat# 4413, RRID: AB_10694110; Beverly, MA, USA,) or Alex Fluor 488-conjugated goat anti-mouse IgG H+L (1:2000; Cell Signaling Technology Cat# 4408, RRID: AB_10694704) in the dark for 1 hour at room temperature. Finally, the sections were stained with DAPI, rinsed with PBS, and observed using a fluorescence microscope. The percentages of NF200- and S100-positive cells were analyzed with Image-Pro Plus 6.0 software. The microvessel density was determined by counting the number of microvessels in each microscopic field.

Statistical analysis

No statistical methods were used to predetermine sample sizes; however, our sample sizes are similar to those reported in previous publications (Rao et al., 2020; Yao et al., 2021). No animals or data points were excluded from the analyses. The assessments were conducted using the blind method. The data were analyzed by one-way analysis of variance using SPSS 19.0 software (IBM, Armonk, NY, USA). After one-way analysis of variance analyses, Bonferroni's *post hoc* test was performed. A $P < 0.05$ indicated statistical significance.

Results

The characterization of BMSCs and BMSC-derived EVs

The multidirectional differentiation ability of BMSCs was examined, including adipogenic differentiation by oil red O staining, osteogenic differentiation by alizarin red S staining, and chondrogenic differentiation by alcian blue staining (**Figure 2A**). The results showed that the BMSCs were able to differentiate into adipocytes, osteocytes, and chondrocytes. The BMSC phenotypes were examined by flow cytometry (**Figure 2B**). The cells were positive for the mesenchymal stem cell markers CD29, CD90, and CD44 and negative for CD34 and CD45, which demonstrated that the cells extracted from the rat bone marrow were BMSCs.

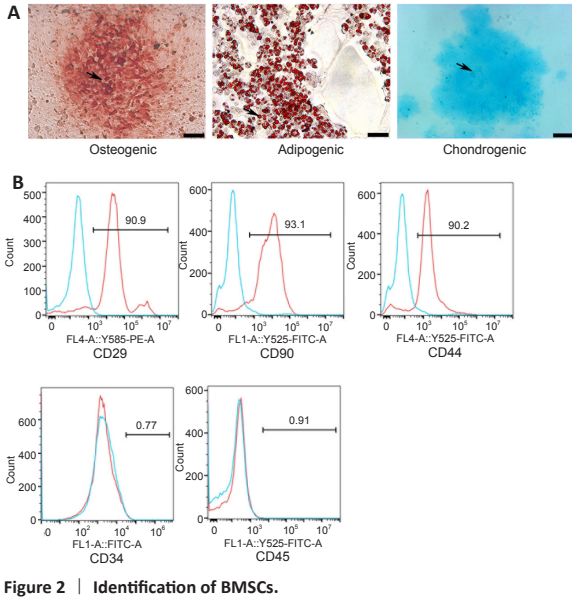

Figure 2 | **Identification of BMSCs.**
(A) BMSCs differentiated into osteoblasts (arrow, stained with alizarin red), adipocytes (arrow, stained with oil red O), and chondrocytes (arrow, stained with alcian blue). Scale bars: 20 μm. (B) BMSC characterization using flow cytometry. The cells were positive for CD90, CD29, and CD44 and negative for CD34 and CD45. BMSC: Bone marrow mesenchymal stem cell.

BMSC-derived EVs were isolated from the cell supernatants with a final concentration of 1135 μg/mL. The EVs were observed by transmission electron microscopy and showed a typical cup-shaped morphology (**Figure 3A**). Nanoparticle tracking analysis revealed that the diameters of the EVs

mainly ranged from 30–200 nm (**Figure 3B**). Expression of the EV surface markers CD9 and TSG101 was positive by western blot (**Figure 4C**). We characterized the particles by their appearance, particle size, and surface markers, and the isolated particles demonstrated the features of EVs.

The uptake of BMSC-derived EVs by HUVECs

To examine the uptake of BMSC-derived EVs *in vitro*, we labeled the EVs and tracked them successfully after engulfment by HUVECs. After a 24-hour coculture with HUVECs, **Figure 3D** clearly shows that EVs were present within the cytoplasm of the HUVECs. Tube formation assays were used to determine the pro-angiogenic effect of BMSC-derived EVs. The assays showed that the addition of EVs promoted an increase in tube lengths, and the EVs from 2-day-old rat BMSCs performed significantly better than EVs from 8-week-old rat BMSCs (**Figure 3E** and **F**).

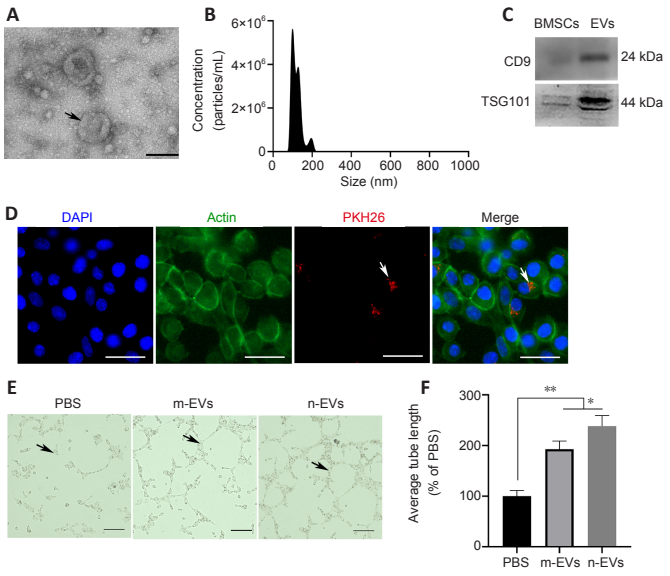

Figure 3 | Identification of BMSC-derived EVs and effect of the EVs on tube formation by human umbilical vein endothelial cells (HUVECs).

(A) Electron-microscopic observation of BMSC-derived EVs. The EVs (arrow) exhibited a cup-shaped morphology. (B) The size of BMSC-derived EVs was determined by nanoparticle tracking analysis. (C) Western blot analysis indicated that EVs were positive for the surface markers CD9 and TSG101. (D) HUVECs (arrows) were stained green with Actin-Tracker Green and BMSC-derived EVs were stained red with PKH26. The EVs were engulfed by HUVECs. (E) Tube formation (arrows) by HUVECs. Angiogenic networks revealed that the n-EV group exhibited the longest average tube length, and the tube length in the m-EV group was longer than that in the PBS group. Scale bars: 100 nm in A, 30 μm in D, and 200 μm in E. (F) Quantitative results of the average tube lengths. Data are expressed as means ± SEM (n = 3). The experiments were repeated three times. *P < 0.05, **P < 0.01 (one-way analysis of variance followed by Bonferroni's *post hoc* test). BMSCs: Bone mesenchymal stem cells; DAPI: 4′,6-diamidino-2-phenylindole; EVs: extracellular vesicles; m-EVs: EVs from 8-week-old rats BMSCs; n-EVs: EVs from 2-day-old rats BMSCs; PBS: phosphate-buffered saline; TSG101: tumor susceptibility gene 101.

Loading rGO-GelMA-PCL nerve conduits with BMSC-derived EVs improves the electrophysiology and motor function of rats with nerve defects

The electrical conduction of regenerated nerves and the reinnervation of the muscles were detected using electrophysiological methods (**Figure 4A**). The amplitude of compound muscle action potential in the EV group was higher than that in the control group, which indicated that the addition of EVs improved muscle reinnervation; however, the autograft group displayed a higher amplitude than both the control and EV groups (**Figure 4B**). The motor nerve conduction velocity was higher in the EV group than that in the control group, which indicated that the addition of EVs improved myelin sheath recovery, and the velocity in the EV group was not significantly different from that in the autograft group (**Figure 4C**).

After sciatic nerve injury, the central nervous system loses control of the muscles in the operated side, which influences the gait of the rats. Therefore, gait analysis was used to evaluate the motor function of the regenerated nerves. **Figure 4D** shows that the static parameters (sciatic function index) of the EV group were higher than those of the control group (P < 0.01) and were lower than those in the autograft group (P > 0.05).

Loading rGO-GelMA-PCL nerve conduits with BMSC-derived EVs improves gastrocnemius muscle recovery in rats with nerve defects

Denervated muscles lose signal transmission from the nervous system and are unable to maintain contraction function. Consequently, the diameter of the muscles decreases and myatrophy occurs (Rochkind et al., 2013; Xiang et al., 2021). Twelve weeks after surgery, the gastrocnemius muscles from the operated and contralateral sides were dissected. Microscopic cross-sections of gastrocnemius muscles stained with Masson's trichrome solutions were recorded, and the cross-sectional areas of muscle fibers were determined (**Figure 5A** and **B**). The mean cross-sectional area of the muscle fibers indicated that the muscles maintained their size to a greater extent in the EV group than in the control group (P < 0.01). **Figure 5C** demonstrates that the gastrocnemius muscle wet weight ratios (operated/contralateral side) in the EV group were greater than those in the control group, and there was no significant difference between the autograft and EV groups (P > 0.05).

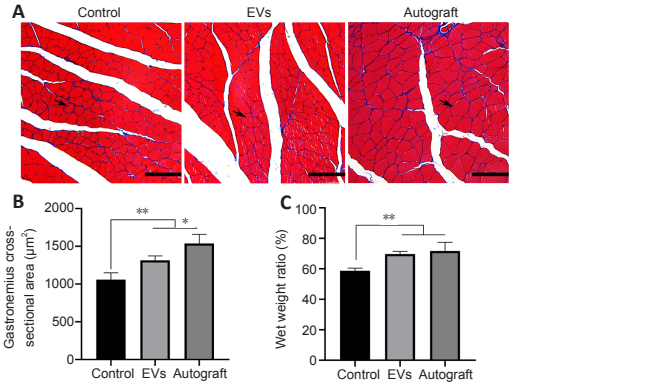

Figure 4 | Effect of loading rGO-GelMA-PCL nerve conduits with BMSC-derived EVs on sciatic nerve functional recovery in rats with nerve defects at 12 weeks after surgery.

(A) Representative CMAP recordings from the operated limb. CMAP amplitude was highest in the autograft group and lowest in the control group. (B) CMAP amplitudes. (C) Motor nerve conduction velocity. MNCV in the EV group was similar to that in the autograft group, which were both higher than that in the control group. (D) Evaluation of sciatic nerve functional recovery using the SFI. The SFI was highest in the autograft group, and the SFI in the EV group was higher than that in the control group. Data are expressed as means ± SEM (n = 4). *P < 0.05, **P < 0.01 (one-way analysis of variance followed by Bonferroni's *post hoc* test). BMSC: Bone mesenchymal stem cells; CMAP: compound muscle action potential; EVs: extracellular vesicles; MNCV: motor nerve conduction velocity; rGO-GelMA-PCL: reduced graphene oxide with gelatin-methacryloyl and polycaprolactone; SFI: sciatic function index.

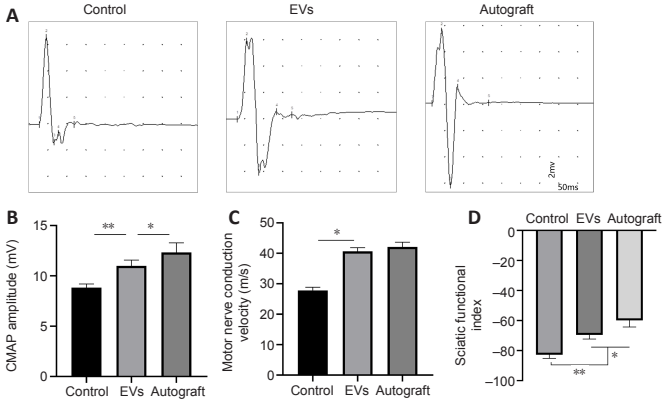

Figure 5 | Effect of loading rGO-GelMA-PCL nerve conduits with BMSC-derived EVs on the gastrocnemius muscles from the operated and contralateral sides of rats with nerve defects at 12 weeks after surgery.

(A) Masson's trichrome stained images of transverse sections of the gastrocnemius muscles. Muscle fibers (arrows) are shown in red with the largest fibers in the autograft group. The fibers in the EV group were larger than those in the control group. Scale bars: 100 μm. (B, C) Quantitative results of gastrocnemius cross-sectional areas and wet weight ratios (operated/contralateral side). (D) Quantitative results of sciatic functional index in each group. Higher values of sciatic functional index mean better nerve function. Data are expressed as mean ± SEM (n = 4). **P < 0.01 (one-way analysis of variance followed by Bonferroni's *post hoc* test). BMSC: Bone mesenchymal stem cells; EVs: extracellular vesicles; rGO-GelMA-PCL: reduced graphene oxide with gelatin-methacryloyl and polycaprolactone.

Loading rGO-GelMA-PCL nerve conduits with BMSC-derived EVs improves the micro-structure of the regenerated nerves in rats with nerve defects

The ultra-structure of the regenerated nerve was evaluated by transmission electron microscopy (**Figure 6A**), the myelin sheaths were stained with toluidine blue (**Figure 6B**), and the gross numbers of the regenerated nerve fibers were counted (**Figure 6C**). Cross sections of the middle part of the regenerated nerve showed that the nerve fiber density for each group was different. The density of myelinated nerve fibers in the EV group was higher than that in the control group, and no difference was observed between the EV and autograft groups (P > 0.05).

In **Figure 6A**, each regenerated axon was covered with a myelin sheath, although sheath thickness differed among the groups. The regenerated sheaths in the EV group were thicker than those in the control group and similar to those in the autograft group (P > 0.05), which illustrated the positive effect of BMSC-derived EVs on Schwann cells surrounding the nerve fibers. Moreover, the diameter of myelinated axons in the EV group was also higher than that in the control group, and there was no significant difference between the EV and autograft groups (**Figure 6D** and **E**).

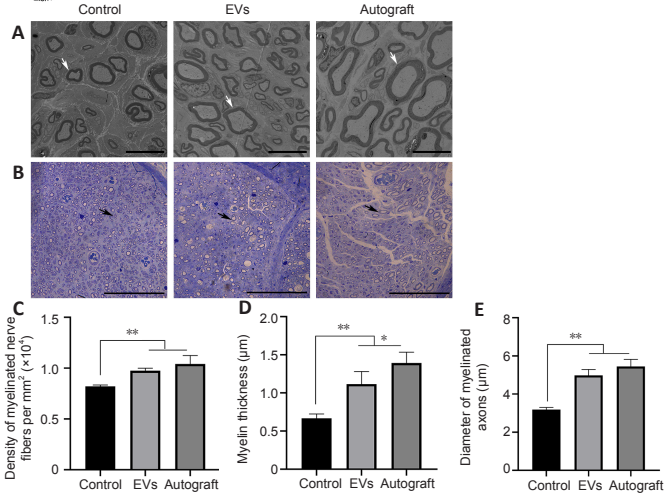

Figure 6 | Effect of loading rGO-GelMA-PCL nerve conduits with BMSC-derived EVs on regenerated nerve microstructure in rats with nerve defects.
(A) Transmission electron microscopy images of regenerated sciatic nerves. Both the myelin (arrows) thicknesses and diameters of myelinated axons were highest in the autograft group and lowest in the control group. The diameters of myelinated axons in the EV group were similar to those in the autograft group. (B) Toluidine blue staining of regenerated sciatic nerves. The densities of myelinated axons (arrows) in the EV group were similar to those in the autograft group, which were both higher than those in the control group. Scale bars: 5 μm in A and 20 μm in B. (C–E) Quantitative results of the densities of myelinated axons (C), thicknesses of myelinated sheaths (D), and diameters of myelinated axons (E). Data are expressed as means ± SEM (n = 4). *P < 0.05, **P < 0.01 (one-way analysis of variance followed by Bonferroni's *post hoc* test). BMSC: Bone mesenchymal stem cells; EVs: extracellular vesicles; rGO-GelMA-PCL: reduced graphene oxide with gelatin-methacryloyl and polycaprolactone.

Loading rGO-GelMA-PCL nerve conduits with BMSC-derived EVs improves recovery of regenerated nerves in rats with nerve defects

Double NF200/S100 immunofluorescent staining of the middle part of the grafts showed that both axons and myelin sheaths had migrated from the proximal nerve stump to the distal nerve stump at 12 weeks after surgery. The percentages of NF200- and S100-positive areas in the EV group were demonstrably higher than those in the control group, and the percentages of S100-positive areas were similar for the EV and autograft groups (P > 0.05; **Figure 7**).

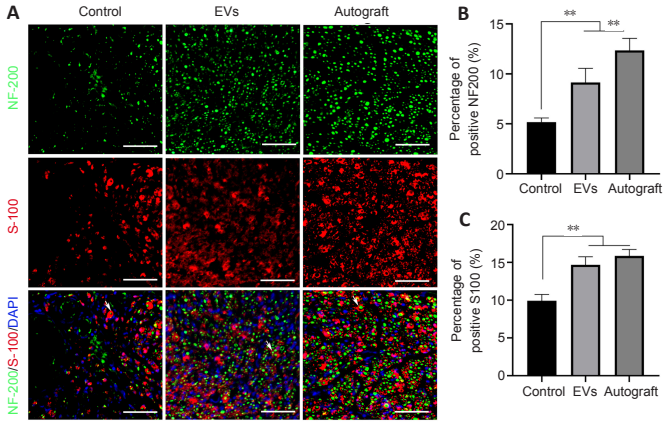

Figure 7 | rGO-GelMA-PCL nerve conduits loaded with BMSC-derived EVs promotes the regeneration of sciatic nerves at 12 weeks after surgery.
(A) Double NF200 (green, stained with Alexa Fluor® 488)/S100 (red, stained with Alexa Fluor® 555) immunofluorescent staining of the middle sections of the regenerated nerves (arrows). The cell nuclei were stained blue with DAPI. The myelin sheaths were stained red and enclosed axons were stained green. The percentages of NF200-positive cells were highest in the autograft group and lowest in the control group, and the percentages of S100-positive cells in the EVs group were higher than those in the control group. The percentage of S100-positive cells in the EV group was similar to that in the autograft group. Scale bars: 50 μm. (B, C) Quantitative results of the percentages of NF200- and S100-positive areas. Data are expressed as means ± SEM (n = 4). **P < 0.01 (one-way analysis of variance followed by Bonferroni's *post hoc* test). BMSC: Bone mesenchymal stem cells; DAPI: 4′,6-diamidino-2-phenylindole ; EVs: extracellular vesicles; NF200: neurofilament 200; rGO-GelMA-PCL: reduced graphene oxide with gelatin-methacryloyl and polycaprolactone.

Angiogenesis plays an important role in the process of tissue regeneration (Gonçalves et al., 2021). Statistical analysis showed that microvessel density in the EV group was significantly higher than that in the control group (P < 0.01) and was similar to that in the autograft group (P > 0.05; **Figure 8**).

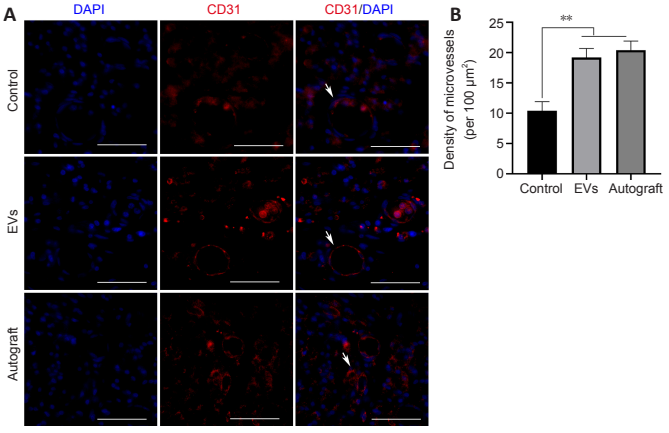

Figure 8 | rGO-GelMA-PCL nerve conduits loaded with BMSC-derived EVs improve angiogenesis in rats with nerve defects at 12 weeks after surgery.
(A) CD31 (red, stained with Alexa Fluor® 555) immunofluorescent staining of regenerated nerves. The microvessels (CD31, arrows) were stained red, and the nuclei were stained blue with DAPI. The densities of microvessels in the EV group were similar to those in the autograft group and were both higher than those in the control group. Scale bars: 50 μm. (B) Quantitative results of microvessel density. Data are expressed as means ± SEM (n = 4). **P < 0.01 (one-way analysis of variance followed by Bonferroni's *post hoc* test). BMSC: Bone mesenchymal stem cells; DAPI: 4′,6-diamidino-2-phenylindole; EVs: extracellular vesicles; rGO-GelMA-PCL: reduced graphene oxide with gelatin-methacryloyl and polycaprolactone.

Discussion

The peripheral nervous system is capable of regeneration after injury (Scheib and Höke, 2013; He and Jin, 2016). However, the regenerative ability is limited when the nerve damage is too great (Li et al., 2014). In this study, we combined BMSC-derived EVs with rGO-GelMA-PCL nerve conduits to promote nerve regeneration and functional recovery in rats with sciatic nerve defects. The key results of this study were the increases in myelinated nerve fiber diameter and myelin sheath thickness that were observed in the EV group compared with the rats that received only the rGO-GelMA-PCL nerve conduit (control group). Furthermore, our results showed that the addition of EVs to the conduit improved nerve function compared with using the conduit alone for nerve repair.

Previous experiments showed that BMSCs displayed stronger vitality, proliferation potential, and antioxidant capacity when isolated from younger donors (Mueller and Glowacki, 2001; Stenderup et al., 2003). With age, telomeres of cells are gradually depleted, and long-term contact between mitochondrial DNA and reactive oxygen species causes mitochondrial dysfunction, resulting in increased potential for DNA mutations and changes in epigenetic inheritance (Yu and Kang, 2013). In this study, BMSCs were obtained from the bone marrow of newborn rats to obtain the best repair results. The disadvantage of this study design is that it is not possible to obtain neonatal BMSCs for clinical use; however, umbilical cord blood-derived MSCs may be an alternative source for nerve repair (Kern et al., 2006).

In a previous study, MSC-derived EVs from young and aged individuals played different roles in alleviating acute lung injury, which may have been related to EV internalization and miRNA content changes (Huang et al., 2019). In the current study, we found that neonatal BMSCs-derived EVs promoted angiogenesis to a greater extent than those from young mice. In one study, EVs were applied by different methods, such as through intravenous injection and direct application to the injured area (Mead and Tomarev, 2017). Intravenous injection requires a larger amount of EVs (over 100 μg) than direct local application and relies on delivery through the blood system to the site of injury to function (Grange et al., 2019; Ma et al., 2019; Xiao et al., 2021). In this process, EVs pass through the lungs and remain in other organs, which greatly reduces the number of EVs that reach the target site (Guo et al., 2019). In our experiments, we chose to combine EVs with the nerve conduit, which directly acted at the damaged site and improved the transport efficiency. Previous studies have shown that the local application of a small dose of EVs (less than 20 μg) had a significant therapeutic effect on wound healing and lung injury (Zhu et al., 2014; Duan et al., 2020). In this study, considering the limitation of the space within the conduit, the amount of EVs was controlled at 20 μg.

A series of previous studies demonstrated that tissue-engineered nerve conduits were a promising approach for nerve regeneration therapy (Li et al., 2020; Wang et al., 2020a, b). The physical connection of the nerve stumps can guide the direction of axonal sprouting and reduce scar tissue formation (Houshyar et al., 2019). However, our focus was on finding superior biomaterials, and we expected to find methods to enhance existing conduits to promote nerve regeneration. Nerve conduits combined with BMSC-derived EVs were simple to generate, and our results indicated that combining tissue-engineered nerve conduits and BMSC-derived EVs significantly promoted nerve regeneration and functional recovery compared with nerve conduits alone. Our previous study found that rGO-GelMA-PCL nerve conduits

displayed excellent biocompatibility and mechanical properties and promoted epithelial-mesenchymal transition of Schwann cells and axon extension *in vitro* (Fang et al., 2020a). In addition, miRNA contained in MSC-derived EVs was shown to regulate angiogenesis and promote injury regeneration; miR-125a was transferred into endothelial cells and then promoted angiogenesis by repressing delta-like ligand 4 expression (Liang et al., 2016). Our results also showed that the EV group produced more angiogenesis than the control group. More importantly, the EV group regenerated thicker myelin sheaths and produced larger myelinated nerve fiber diameters than the control group, possibly because of an improved blood supply from angiogenic induction, which ultimately promoted nerve regeneration. The improvement in nerve regeneration led to increased neural function, including improved neural electrophysiology and sciatic function index performance.

The results of our study confirmed that BMSC-derived EVs combined with the rGO-GelMA-PCL nerve conduit promoted nerve regeneration, likely because of the pro-angiogenic effect of the EVs and EV-mediated promotion of Schwann cell proliferation within the rGO-GelMA-PCL conduit. Furthermore, our results showed that BMSCs-derived EVs can replace BMSCs to promote nerve regeneration. However, it should be noted that this study concentrated on only the pro-angiogenesis effect of the EVs, which may also promote nerve regeneration by anti-apoptotic and anti-inflammatory mechanisms. Therefore, further investigations should focus on the mechanisms by which BMSC-derived EVs promote nerve regeneration and methods to strengthen the cooperation between EVs and nerve conduits to promote nerve regrowth. However, there are differences in nerve regeneration between rats and humans. In rats, for example, nerve regeneration occurs at a rate of 3 mm per day compared with 1 mm per day in humans (Gordon, 2016). Furthermore, the diameters and lengths of human peripheral nerves are significantly greater than those of rats. As a result, the length of nerve defects in humans is often longer than that in a rat model, and the maximum effective space for nerve conduits currently used in humans is approximately 25 mm (Kasper et al., 2020). How to overcome these differences and apply EV-loaded nerve conduits in the clinic will require further investigations.

In this study, we successfully combined BMSC-derived EVs with rGO-GelMA-PCL nerve conduits to achieve a better therapeutic effect for sciatic nerve defects. *In vitro*, BMSC-derived EVs were engulfed by HUVECs and promoted tube formation. *In vivo*, our results demonstrated that BMSC-derived EVs could combine with rGO-GelMA-PCL nerve conduits to promote sciatic nerve repair by stimulating angiogenesis. In conclusion, BMSC-derived EVs combined with rGO-GelMA-PCL nerve conduits have development potential as a treatment option for patients with peripheral nerve defects.

Author contributions: *Study design and manuscript review: NH; manuscript writing: WZ; study implementation and data analysis: WZ, XXF, QCL, WP. All authors approved the final version of this paper.*
Conflicts of interest: *All authors declare that they have no conflict of interest or financial conflicts to disclose.*
Availability of data and materials: *All data generated or analyzed during this study are included in this published article and its supplementary information files.*
Open access statement: *This is an open access journal, and articles are distributed under the terms of the Creative Commons AttributionNonCommercial-ShareAlike 4.0 License, which allows others to remix, tweak, and build upon the work non-commercially, as long as appropriate credit is given and the new creations are licensed under the identical terms.*
Open peer reviewers: *Yu-Bao Lu, The Third Affiliated Hospital, Sun Yet-sun University, China; Jun-Xuan Ma, AO Research Institute Davos, Switzerland; Maria Easler, University of Padova, Italy.*
Additional file: *Open peer review reports 1–3.*

References

Adameyko I, Ernfors P (2019) Nerves do it again: donation of mesenchymal cells for tissue regeneration. Cell Stem Cell 24:195-197.

Breitbach M, Bostani T, Roell W, Xia Y, Dewald O, Nygren JM, Fries JW, Tiemann K, Bohlen H, Hescheler J, Welz A, Bloch W, Jacobsen SE, Fleischmann BK (2007) Potential risks of bone marrow cell transplantation into infarcted hearts. Blood 110:1362-1369.

Brennan MÁ, Layrolle P, Mooney DJ (2020) Biomaterials functionalized with MSC secreted extracellular vesicles and soluble factors for tissue regeneration. Adv Funct Mater 30:1909125.

Bueno A, Carvalho FB, Gutierres JM, Lhamas C, Andrade CM (2017) A comparative study of the effect of the dose and exposure duration of anabolic androgenic steroids on behavior, cholinergic regulation, and oxidative stress in rats. PLoS One 12:e0177623.

Dong X, Liu S, Yang Y, Gao S, Li W, Cao J, Wan Y, Huang Z, Fan G, Chen Q, Wang H, Zhu M, Kong D (2021) Aligned microfiber-induced macrophage polarization to guide schwann-cell-enabled peripheral nerve regeneration. Biomaterials 272:120767.

Duan M, Zhang Y, Zhang H, Meng Y, Qian M, Zhang G (2020) Epidermal stem cell-derived exosomes promote skin regeneration by downregulating transforming growth factor-β1 in wound healing. Stem Cell Res Ther 11:452.

Duarte-Moreira RJ, Castro KV, Luz-Santos C, Martins JVP, Sá KN, Baptista AF (2018) Electromyographic biofeedback in motor function recovery after peripheral nerve injury: an integrative review of the literature. Appl Psychophysiol Biofeedback 43:247-257.

Erdal AI, Findikçioğlu K, Karasu O, Özkoçer SE, Elmas Ç (2022) Use of erythropoietin and fibrin glue mixture for peripheral nerve repair. Plast Reconstr Surg 149:395-403.

Fang X, Guo H, Zhang W, Fang H, Li Q, Bai S, Zhang P (2020a) Reduced graphene oxide-GelMA-PCL hybrid nanofibers for peripheral nerve regeneration. J Mater Chem B 8:10593-10601.

Fang X, Deng J, Zhang W, Guo H, Yu F, Rao F, Li Q, Zhang P, Bai S, Jiang B (2020b) Conductive conduit small gap tubulization for peripheral nerve repair. RSC Adv 10:16769-16775.

Farokhi M, Mottaghitalab F, Saeb MR, Shojaei S, Zarrin NK, Thomas S, Ramakrishna S (2021) Conductive biomaterials as substrates for neural stem cells differentiation towards neuronal lineage cells. Macromol Biosci 21:e2000123.

Geetha Bai R, Ninan N, Muthoosamy K, Manickam S (2018) Graphene: A versatile platform for nanotheranostics and tissue engineering. Prog Mater Sci 91:24-69.

Gonçalves RC, Banfi A, Oliveira MB, Mano JF (2021) Strategies for re-vascularization and promotion of angiogenesis in trauma and disease. Biomaterials 269:120628.

Gordon T (2016) Electrical stimulation to enhance axon regeneration after peripheral nerve injuries in animal models and humans. Neurotherapeutics 13:295-310.

Grange C, Skovronova R, Marabese F, Bussolati B (2019) Stem cell-derived extracellular vesicles and kidney regeneration. Cells 8:1240.

Griffin JW, Hogan MV, Chhabra AB, Deal DN (2013) Peripheral nerve repair and reconstruction. J Bone Joint Surg Am 95:2144-2151.

Guo S, Perets N, Betzer O, Ben-Shaul S, Sheinin A, Michaelevski I, Popovtzer R, Offen D, Levenberg S (2019) Intranasal delivery of mesenchymal stem cell derived exosomes loaded with phosphatase and tensin homolog siRNA repairs complete spinal cord injury. ACS Nano 13:10015-10028.

He L, He T, Xing J, Zhou Q, Fan L, Liu C, Chen Y, Wu D, Tian Z, Liu B, Rong L (2020) Bone marrow mesenchymal stem cell-derived exosomes protect cartilage damage and relieve knee osteoarthritis pain in a rat model of osteoarthritis. Stem Cell Res Ther 11:276.

He Z, Jin Y (2016) Intrinsic control of axon regeneration. Neuron 90:437-451.

Houshyar S, Bhattacharyya A, Shanks R (2019) Peripheral nerve conduit: materials and structures. ACS Chem Neurosci 10:3349-3365.

Huang R, Qin C, Wang J, Hu Y, Zheng G, Qiu G, Ge M, Tao H, Shu Q, Xu J (2019) Differential effects of extracellular vesicles from aging and young mesenchymal stem cells in acute lung injury. Aging (Albany NY) 11:7996-8014.

Kasper M, Deister C, Beck F, Schmidt CE (2020) Bench-to-bedside lessons learned: commercialization of an acellular nerve graft. Adv Healthc Mater 9:e2000174.

Kern S, Eichler H, Stoeve J, Klüter H, Bieback K (2006) Comparative analysis of mesenchymal stem cells from bone marrow, umbilical cord blood, or adipose tissue. Stem Cells 24:1294-1301.

Khayat A, Monteiro N, Smith EE, Pagni S, Zhang W, Khademhosseini A, Yelick PC (2017) GelMA-encapsulated hDPSCs and HUVECs for dental pulp regeneration. J Dent Res 96:192-199.

Kim HY, Kim TJ, Kang L, Kim YJ, Kang MK, Kim J, Ryu JH, Hyeon T, Yoon BW, Ko SB, Kim BS (2020) Mesenchymal stem cell-derived magnetic extracellular nanovesicles for targeting and treatment of ischemic stroke. Biomaterials 243:119942.

Lee J, Manoharan V, Cheung L, Lee S, Cha BH, Newman P, Farzad R, Mehrotra S, Zhang K, Khan F, Ghaderi M, Lin YD, Aftab S, Mostafalu P, Miscuglio M, Li J, Mandal BB, Hussain MA, Wan KT, Tang XS, et al. (2019) Nanoparticle-based hybrid scaffolds for deciphering the role of multimodal cues in cardiac tissue engineering. ACS Nano 13:12525-12539.

Li A, Hokugo A, Yalom A, Berns EJ, Stephanopoulos N, McClendon MT, Segovia LA, Spigelman I, Stupp SI, Jarrahy R (2014) A bioengineered peripheral nerve construct using aligned peptide amphiphile nanofibers. Biomaterials 35:8780-8790.

Li BB, Yin YX, Yan QJ, Wang XY, Li SP (2016) A novel bioactive nerve conduit for the repair of peripheral nerve injury. Neural Regen Res 11:150-155.

Li C, Liu SY, Pi W, Zhang PX (2021) Cortical plasticity and nerve regeneration after peripheral nerve injury. Neural Regen Res 16:1518-1523.

Li X, Yang W, Xie H, Wang J, Zhang L, Wang Z, Wang L (2020) CNT/sericin conductive nerve guidance conduit promotes functional recovery of transected peripheral nerve injury in a rat model. ACS Appl Mater Interfaces 12:36860-36872.

Liang X, Zhang L, Wang S, Han Q, Zhao RC (2016) Exosomes secreted by mesenchymal stem cells promote endothelial cell angiogenesis by transferring miR-125a. J Cell Sci 129:2182-2189.

Liu X, Miller AL, 2nd, Park S, Waletzki BE, Zhou Z, Terzic A, Lu L (2017) Functionalized carbon nanotube and graphene oxide embedded electrically conductive hydrogel synergistically stimulates nerve cell differentiation. ACS Appl Mater Interfaces 9:14677-14690.

Ma Y, Dong L, Zhou D, Li L, Zhang W, Zhen Y, Wang T, Su J, Chen D, Mao C, Wang X (2019) Extracellular vesicles from human umbilical cord mesenchymal stem cells improve nerve regeneration after sciatic nerve transection in rats. J Cell Mol Med 23:2822-2835.

McCaig CD, Rajnicek AM, Song B, Zhao M (2005) Controlling cell behavior electrically: current views and future potential. Physiol Rev 85:943-978.

Mead B, Tomarev S (2017) Bone marrow-derived mesenchymal stem cells-derived exosomes promote survival of retinal ganglion cells through miRNA-dependent mechanisms. Stem Cells Transl Med 6:1273-1285.

Mueller SM, Glowacki J (2001) Age-related decline in the osteogenic potential of human bone marrow cells cultured in three-dimensional collagen sponges. J Cell Biochem 82:583-590.

Percie du Sert N, Hurst V, Ahluwalia A, Alam S, Avey MT, Baker M, Browne WJ, Clark A, Cuthill IC, Dirnagl U, Emerson M, Garner P, Holgate ST, Howells DW, Karp NA, Lazic SE, Lidster K, MacCallum CJ, Macleod M, Pearl EJ, et al. (2020) The ARRIVE guidelines 2.0: Updated guidelines for reporting animal research. PLoS Biol 18:e3000410.

Phinney DG, Pittenger MF (2017) Concise review: MSC-derived exosomes for cell-free therapy. Stem Cells 35:851-858.

Pozzobon LG, Sperling LE, Teixeira CE, Malysz T, Pranke P (2021) Development of a conduit of PLGA-gelatin aligned nanofibers produced by electrospinning for peripheral nerve regeneration. Chem Biol Interact 348:109621.

Qu WR, Zhu Z, Liu J, Song DB, Tian H, Chen BP, Li R, Deng LX (2021) Interaction between Schwann cells and other cells during repair of peripheral nerve injury. Neural Regen Res 16:93-98.

Rani S, Ritter T (2016) The exosome- a naturally secreted nanoparticle and its application to wound healing. Adv Mater 28:5542-5552.

Rao F, Zhang D, Fang T, Lu C, Wang B, Ding X, Wei S, Zhang Y, Pi W, Xu H, Wang Y, Jiang B, Zhang P (2019) Exosomes from human gingiva-derived mesenchymal stem cells combined with biodegradable chitin conduits promote rat sciatic nerve regeneration. Stem Cells Int 2019:2546367.

Rao F, Wang Y, Zhang D, Lu C, Cao Z, Sui J, Wu M, Zhang Y, Pi W, Wang B, Kou Y, Wang X, Zhang P, Jiang B (2020) Aligned chitosan nanofiber hydrogel grafted with peptides mimicking bioactive brain-derived neurotrophic factor and vascular endothelial growth factor repair long-distance sciatic nerve defects in rats. Theranostics 10:1590-1603.

Rochkind S, Geuna S, Shainberg A (2013) Phototherapy and nerve injury: focus on muscle response. Int Rev Neurobiol 109:99-109.

Saeki M, Tanaka K, Imatani J, Okamoto H, Watanabe K, Nakamura T, Gotani H, Ohi H, Nakamura R, Hirata H (2018) Efficacy and safety of novel collagen conduits filled with collagen filaments to treat patients with peripheral nerve injury: A multicenter, controlled, open-label clinical trial. Injury 49:766-774.

Scheib J, Höke A (2013) Advances in peripheral nerve regeneration. Nat Rev Neurol 9:668-676.

Siddiqui N, Asawa S, Birru B, Baadhe R, Rao S (2018) PCL-based composite scaffold matrices for tissue engineering applications. Mol Biotechnol 60:506-532.

Sinis N, Haerle M, Becker ST, Schulte-Eversum C, Vonthein R, Rösner H, Schaller HE (2007) Neuroma formation in a rat median nerve model: influence of distal stump and muscular coating. Plast Reconstr Surg 119:960-966.

Stenderup K, Justesen J, Clausen C, Kassem M (2003) Aging is associated with decreased maximal life span and accelerated senescence of bone marrow stromal cells. Bone 33:919-926.

Sun L, Xu R, Sun X, Duan Y, Han Y, Zhao Y, Qian H, Zhu W, Xu W (2016) Safety evaluation of exosomes derived from human umbilical cord mesenchymal stromal cell. Cytotherapy 18:413-422.

Sun M, Wang S, Li Y, Yu L, Gu F, Wang C, Yao Y (2013) Adipose-derived stem cells improved mouse ovary function after chemotherapy-induced ovary failure. Stem Cell Res Ther 4:80.

Théry C, Amigorena S, Raposo G, Clayton A (2006) Isolation and characterization of exosomes from cell culture supernatants and biological fluids. Curr Protoc Cell Biol Chapter 3:Unit 3.22.

Wang J, Cheng Y, Wang H, Wang Y, Zhang K, Fan C, Wang H, Mo X (2020a) Biomimetic and hierarchical nerve conduits from multifunctional nanofibers for guided peripheral nerve regeneration. Acta Biomater 117:180-191.

Wang J, Xiong H, Zhu T, Liu Y, Pan H, Fan C, Zhao X, Lu WW (2020b) Bioinspired multichannel nerve guidance conduit based on shape memory nanofibers for potential application in peripheral nerve repair. ACS Nano 14:12579-12595.

Wang J, Cheng Y, Chen L, Zhu T, Ye K, Jia C, Wang H, Zhu M, Fan C, Mo X (2019) In vitro and in vivo studies of electroactive reduced graphene oxide-modified nanofiber scaffolds for peripheral nerve regeneration. Acta Biomater 84:98-113.

Wang L, Lu C, Yang S, Sun P, Wang Y, Guan Y, Liu S, Cheng D, Meng H, Wang Q, He J, Hou H, Li H, Lu W, Zhao Y, Wang J, Zhu Y, Li Y, Luo D, Li T, et al. (2020c) A fully biodegradable and self-electrified device for neuroregenerative medicine. Sci Adv 6:eabc6686.

Xiang Y, Dai J, Xu L, Li X, Jiang J, Xu J (2021) Research progress in immune microenvironment regulation of muscle atrophy induced by peripheral nerve injury. Life Sci 287:120117.

Xiao X, Li W, Rong D, Xu Z, Zhang Z, Ye H, Xie L, Wu Y, Zhang Y, Wang X (2021) Human umbilical cord mesenchymal stem cells-derived extracellular vesicles facilitate the repair of spinal cord injury via the miR-29b-3p/PTEN/Akt/mTOR axis. Cell Death Discov 7:212.

Xin H, Li Y, Buller B, Katakowski M, Zhang Y, Wang X, Shang X, Zhang ZG, Chopp M (2012) Exosome-mediated transfer of miR-133b from multipotent mesenchymal stromal cells to neural cells contributes to neurite outgrowth. Stem Cells 30:1556-1564.

Xu H, Holzwarth JM, Yan Y, Xu P, Zheng H, Yin Y, Li S, Ma PX (2014) Conductive PPY/PDLLA conduit for peripheral nerve regeneration. Biomaterials 35:225-235.

Xu L, Wang S, Sui X, Wang Y, Su Y, Huang L, Zhang Y, Chen Z, Chen Q, Du H, Zhang Y, Yan L (2017) Mesenchymal stem cell-seeded regenerated silk fibroin complex matrices for liver regeneration in an animal model of acute liver failure. ACS Appl Mater Interfaces 9:14716-14723.

Yao X, Yan Z, Li X, Li Y, Ouyang Y, Fan C (2021) Tacrolimus-induced neurotrophic differentiation of adipose-derived stem cells as novel therapeutic method for peripheral nerve injury. Front Cell Neurosci 15:799151.

Yu B, Zhang X, Li X (2014) Exosomes derived from mesenchymal stem cells. Int J Mol Sci 15:4142-4157.

Yu KR, Kang KS (2013) Aging-related genes in mesenchymal stem cells: a mini-review. Gerontology 59:557-563.

Zaminy A, Sayad-Fathi S, Kasmaie FM, Jahromi Z, Zendedel A (2021) Decellularized peripheral nerve grafts by a modified protocol for repair of rat sciatic nerve injury. Neural Regen Res 16:1086-1092.

Zhang B, Yan W, Zhu Y, Yang W, Le W, Chen B, Zhu R, Cheng L (2018) Nanomaterials in neural-stem-cell-mediated regenerative medicine: imaging and treatment of neurological diseases. Adv Mater 30:e1705694.

Zhang L, Tang Y, Zhu X, Tu T, Sui L, Han Q, Yu L, Meng S, Zheng L, Valverde P, Tang J, Murray D, Zhou X, Drissi H, Dard MM, Tu Q, Chen J (2017) Overexpression of MiR-335-5p promotes bone formation and regeneration in mice. J Bone Miner Res 32:2466-2475.

Zhang Q, Zhao Y, Xu Y, Chen Z, Liu N, Ke C, Liu B, Wu W (2016) Sodium ferulate and n-butylidenephthalate combined with bone marrow stromal cells (BMSCs) improve the therapeutic effects of angiogenesis and neurogenesis after rat focal cerebral ischemia. J Transl Med 14:223.

Zhu W, Huang L, Li Y, Qian H, Shan X, Yan Y, Mao F, Wu X, Xu WR (2011) Mesenchymal stem cell-secreted soluble signaling molecules potentiate tumor growth. Cell Cycle 10:3198-3207.

Zhu YG, Feng XM, Abbott J, Fang XH, Hao Q, Monsel A, Qu JM, Matthay MA, Lee JW (2014) Human mesenchymal stem cell microvesicles for treatment of Escherichia coli endotoxin-induced acute lung injury in mice. Stem Cells 32:116-125.

Zou Y, Ma D, Shen H, Zhao Y, Xu B, Fan Y, Sun Z, Chen B, Xue W, Shi Y, Xiao Z, Gu R, Dai J (2020) Aligned collagen scaffold combination with human spinal cord-derived neural stem cells to improve spinal cord injury repair. Biomater Sci 8:5145-5156.

P-Reviewers: Lu Y, Ma J, Easler M; C-Editor: Zhao M; S-Editors: Yu J, Li CH; L-Editors: Zunino S, Yu J, Song LP; T-Editor: Jia Y